Nano Energy 91 (2022) 106669

Contents lists available at ScienceDirect

Nano Energy

journal homepage: www.elsevier.com/locate/nanoen

Regulating the Li_2S deposition by grain boundaries in metal nitrides for stable lithium-sulfur batteries

Jin-Lin Yang [a,b], Da-Qian Cai [a,b], Qiaowei Lin [a], Xin-Yu Wang [a,b], Zou-Qiang Fang [a,b], Ling Huang [a], Zhi-Jie Wang [c], Xiao-Ge Hao [a,b], Shi-Xi Zhao [a,*], Jia Li [c,*], Guo-Zhong Cao [d], Wei Lv [a,*]

[a] Shenzhen Geim Graphene Center, Engineering Laboratory for Functionalized Carbon Materials, Tsinghua Shenzhen International Graduate School, Tsinghua University, Shenzhen 518055, China
[b] School of Materials Science and Engineering, Tsinghua University, Beijing 100086, China
[c] Guangdong Provincial Key Laboratory of Thermal Management Engineering and Materials and Institute of Materials Research, Tsinghua Shenzhen International Graduate School, Tsinghua University, Shenzhen 518055, China
[d] Department of Materials Science and Engineering, University of Washington, Seattle, WA 98195, USA

ARTICLE INFO

Keywords:
Lithium-sulfur batteries
Grain boundaries
Li_2S nucleation
Redox kinetics
Interlayer

ABSTRACT

Catalysis is a fundamental solution in suppressing the shuttling of lithium polysulfides (LiPSs), which is essential to the practical applications of lithium-sulfur batteries with high energy density. However, the uncontrollable deposition of electronic and ionic insulative Li_2S always passivates the catalyst surface for the continuous LiPS conversion. Herein, we propose an effective method to regulate Li_2S deposition to avoid the catalyst surface passivation by introducing grain boundaries (GBs) in the catalyst. Hollow microspheres composed of MoN-Mo_2N heterostructure with abundant and highly accessible GBs were prepared as the models. The results show GBs act as the two-dimensional nucleation sites, guiding the fast nucleation and three-dimensional deposition of Li_2S around them, avoiding the formation of dense Li_2S coating on their surface. Thus, the high capacity Li_2S deposition with enhanced conversion kinetics was achieved. The interlayer composed of the above catalyst and carbon nanotube effectively suppresses the shuttling of LiPSs and promotes their fast conversion, leading to a low capacity decay of 0.049% per cycle at 1 C for 800 cycles for the assembled battery. With a higher sulfur loading of 4.7 mg cm^{-2} under 0.5 C, high capacity retention of 77.2% after 200 cycles could also be achieved.

1. Introduction

Lithium-sulfur (Li-S) batteries are one of the most promising next-generation batteries with a much higher theoretical energy density than current lithium-ion batteries [1]. However, the formed lithium polysulfides (LiPSs) intermediates between Li and sulfur easily dissolve in the liquid electrolyte and shuttle from cathode to anode, leading to the fast capacity decay and the difficulty in practical commercialization [2,3]. Even worse, these LiPSs have poor conversion reaction kinetics to the solid products (Li_2S_2/Li_2S), and thus, the commonly used physical confinement and chemical adsorption methods are hard to solve the shuttling problem of LiPSs due to their unavoidable accumulation in the electrolyte. Recently, the catalysis in Li-S batteries attracts great attention because it can effectively accelerate the LiPSs conversion, showing a fundamental solution to suppress the LiPSs accumulation and shuttling in the electrolyte [4–6]. Various catalysts, such as metal oxides, sulfides, nitrides, or their heterostructures, have been widely investigated in Li-S batteries, effectively improving the cycling stability and sulfur utilization [7–10]. However, unlike the traditional catalytic reactions that the products can easily desorb from the catalyst surface, the LiPSs conversion follows a dissolution-precipitation process, and the formed solid Li_2S precipitates will cover the catalyst surface. Previous studies have shown that the uncontrollable Li_2S deposition will passivate the cathode and decrease the sulfur utilization because of their low ionic and electronic conductivities [11]. Thus, the Li_2S deposition process and the morphology will significantly affect the Li^+ ion and electron transport at the electrolyte/electrode interface, and then the continuous LiPS catalytic conversion.

Designing a highly porous host, regulating the electrode surface affinity to LiPSs, and using electrolyte additives are usually used to guide

* Corresponding authors.
E-mail addresses: zhaosx@sz.tsinghua.edu.cn (S.-X. Zhao), li.jia@sz.tsinghua.edu.cn (J. Li), lv.wei@sz.tsinghua.edu.cn (W. Lv).

https://doi.org/10.1016/j.nanoen.2021.106669
Received 7 September 2021; Received in revised form 23 October 2021; Accepted 28 October 2021
Available online 30 October 2021

the Li_2S deposition [12,13]. However, it is hard to tune the Li_2S deposition on most of the catalysts due to their relatively small surface area but strong adsorption ability to LiPSs. Thus, designing the active sites on the catalyst surface to tune the Li_2S deposition morphology becomes critical to improve the catalytic conversion efficiency of LiPSs. Grain boundaries (denoted GBs) are the typical two-dimensional (2D) defects in the crystal structure, which are in a higher disorder and active state than the adjacent crystal phase [14,15]. According to previous reports, GBs in the catalyst play significant roles in regulating the surface electronic structure and enhancing the adsorption ability in catalysis [16–18]. Besides, they can also improve the electron and Li^+ transfer [19–21]. Based on the above two points, it can be speculated that GBs in the catalyst can serve as adsorptive and catalytic sites for LiPSs that can trigger the fast nucleation and growth of Li_2S, and thereby regulating the deposition of Li_2S. Nevertheless, the relationship between the GBs and the catalysis in Li-S batteries has been rarely investigated.

Metal nitrides are typical catalysts in Li-S batteries due to their high conductivity and easy preparation [22]. For example, molybdenum nitride can be easily prepared by the high temperature nitridation of MoO_2 under an NH_3 atmosphere, and the insufficient nitridation will produce a mixture phase of MoN and Mo_2N simultaneously, forming abundant GBs between them. Note that the MoN and Mo_2N have similar conductivity (~4.55×10^6 S m^{-1} for MoN and 1×10^5 S m^{-1} for Mo_2N) [23–25]. Thus, in this work, the molybdenum nitride with controlled nitridation is selected as a typical example to investigate the functions of GBs in regulating the Li_2S deposition. A hollow microsphere composed of MoN-Mo_2N heterostructures with rich GBs (denoted RGB-MN) is prepared in which the porous hollow structure ensures the high accessibility of GBs to the LiPSs. In contrast, a higher temperature nitridation leads to the formation of pure Mo_2N with lean GBs (denoted LGB-MN), which was used as the control sample. The results show the rich GBs provide the two-dimensional nucleation sites and enhance the nucleation rate of Li_2S, resulting in the three-dimensional growth of Li_2S on the catalyst surface and thus leaving the ion diffusion channels for continuous deposition. However, with fewer GBs, the Li_2S tends to grow and coat on the catalyst surface uniformly, which passivates the catalyst surface and therefore hinders the subsequent deposition. As a result, the RGB-MN can effectively enhance the redox reaction kinetics between LiPSs and Li_2S. The assembled Li-S battery with such RGB-MN modified separator exhibited excellent cycling stability (high capacity retention of 60.7% at 1 C over 800 cycles) and rate performance (a high capacity of 698 mAh g^{-1} at 4 C). Even with a high sulfur loading of 4.7 mg cm^{-2}, the battery still showed a high capacity retention of 77.2% at a low current density of 0.5 C for 200 cycles, suggesting high reversibility and sulfur utilization.

2. Experimental section

2.1. Preparation of MoO_2

MoO_2 precursor with hollow sphere structure was prepared by a facile hydrothermal process [26]. Firstly, 0.28 g molybdenyl acetylacetonate ($C_{10}H_{16}MoO_6$) was dissolved in 60 mL n-butyl alcohol by ultrasonication for 30 min. Then, 10 mL of 1 M HNO_3 was added into the above green solution and then stirred for 2 h. After that, the above solution was transferred into a 100 mL Teflon-lined stainless autoclave and kept at 220 °C for 12 h in an oven. The obtained black product (MoO_2 hollow microspheres) was then washed by deionized water and ethanol several times through filtration and finally dried under 60 °C for 12 h.

2.2. Preparation of RGB-MN and LGB-MN

The as-prepared MoO_2 hollow microspheres were calcined under high purity NH_3 atmosphere (99.999%) in a tubular furnace at 720 and 820 °C for 2 h with a heating rate of 3 °C min^{-1} to obtain RGB-MN and LGB-MN, respectively. These products were then passivated in a flowing Ar atmosphere for another 12 h to avoid air oxidation.

2.3. Preparation of modified separators

The slurry coating method was adopted to fabricate the interlayer modified separator. Typically, 240 mg of LGB-MN or RGB-MN, 30 mg of CNT and 15 mg of polyvinylidene difluoride (PVDF) were ground together in an agate mortar with the aid of N-methyl-2-pyrrolidone (NMP). Then, the slurry was coated uniformly on polypropylene (PP) membrane (Celgard 2400) by using a doctor blade. A pure CNT modified PP separator was also prepared for comparison. After dried at 35 °C for 12 h, the functional separators were punched into round plates with a diameter of 19 mm. The areal mass loading was controlled around 0.4 mg cm^{-2}.

2.4. Preparation of sulfur cathode

The sulfur cathode was prepared by mixing Super P and sulfur powder. Typically, 0.12 g of Super P and 0.36 g of sulfur powder were mixed by ball-milling and heated in a tubular furnace at 155 °C for 12 h. Then, the composite was mixed with CNT and PVDF with a mass ratio of 8:1:1 with the addition of NMP to form the cathode slurry, followed by coating on Al foil on a coating machine. The typical areal sulfur mass loading was around 1.0 mg cm^{-2}. The cathodes with high areal sulfur loading over 4 mg cm^{-2} were prepared by using styrene-butadiene rubber (SBR) and carboxymethylcellulose sodium (CMC) mixture as the binder. Typically, 22 mg CMC was firstly dissolved in 2 mL deionized water followed by stirring for 60 min. Then, 43 mg CNT was added into the above mixture and stirred for 90 min. After that, 988 mg Super P and sulfur mixture was carefully added into the obtained solution. After another 2 h stirring, 56 mg SBR was dropped into the solution and stirred for another 30 min. Finally, the as prepared slurry was coated on carbon-coated Al foil uniformly by using a doctor blade and dried in a vacuum oven at 60 °C overnight.

2.5. Materials characterization

The crystal structure and phase purity of samples were identified by X-ray diffraction (XRD, Bruke D8 Advance with Cu Ka radiation, λ = 0.15418 nm, scan rate = 10° min^{-1}). The morphology and surface elemental distribution of the samples were investigated by scanning electron microscopy (SEM, ZEISS SUORA®55) equipped with an energy dispersive spectrometer (EDS). High-resolution transmission electron microscopy (HRTEM, JEOL-201) was conducted to characterize the crystal and lattice structure. X-ray photoelectron spectra (XPS, Thermo Fisher, ESCALAB 250X) were operated to investigate the valence states of the elements. The specific surface area and pore size distribution were inspected by N_2 adsorption analyzer (Micromeritics-ASAP 2020). Thermal gravimetric (TG) analysis was measured under Air flow from room temperature to 700 °C to determine the content of the sulfur.

2.6. Li_2S_6 Symmetric cells Test

The electrodes were prepared by loading a mixture of different catalysts (CNT, RGB-MN or LGB-MN) and PVDF (mass ratio 10:1) on carbon paper with the areal mass loading around 1.0 mg cm^{-2}. Then two identical electrodes were assembled into a 2032-coin cell with the addition of 25 μL polysulfide electrolyte (1 M bis(trifluoromethanesulfonyl)imide (LITFSI), 0.2 M Li_2S_6 in DOL/DME = 1/1 v/v) on each side. The CV test was conducted within a voltage window from − 0.8–0.8 V.

2.7. Li_2S nucleation test

Typically, 50 mg sample (CNT, RGB-MN or LGB-MN) was dispersed in ethanol by ultrasonication and dropped on carbon paper disks (12

mm), and the average mass loading for each disk was around 2.5–3.0 mg cm^{-2}. Then, the as-prepared carbon paper-based disks were used as working electrodes, and lithium foils were served as anodes to assemble the battery with 25 μL catholyte (1 M LITFSI, 0.2 M Li_2S_8 in DOL/DME = 1/1 v/v) added in each cell. The cell was discharged to 2.09 V firstly at the current of 0.134 mA galvanostatically followed by a potentiostatic step under 2.08 V for Li_2S nucleation and growth [27]. The capacity of Li_2S nucleation was calculated by Faraday's law. The electrodes after nucleation test were washed by DOL/DME mixture and dried in Ar-filled glovebox followed by SEM test.

2.8. Li_2S dissolution test

The cell assembly process was the same as that mentioned in the Li_2S nucleation test. The Li_2S_8-based cell was firstly discharged at 0.01 mA to 1.8 V galvanostatically followed by potentiostatic discharging at 1.8 V to guarantee the full transformation of sulfur into solid Li_2S. Then the cells were charged to 2.4 V potentiostatically until the current decreased below 0.01 mA to trigger the oxidation of Li_2S into polysulfides [28]. All the Li_2S deposition capacities were calculated based on the integration of the constant voltage discharge profiles and divided by the amount of sulfur in Li_2S_8 electrolyte in each cell.

2.9. Electrochemical measurements

Typical 2032-coin cells were assembled in a glovebox filled with Ar atmosphere and ultralow water and oxygen content (< 0.01 ppm). The electrolyte (1 M LITFSI in DOL/DME = 1/1 v/v, 2 wt% $LiNO_3$) was added into the cells with the electrolyte/sulfur (E/S) ratio of 15 μL mg^{-1} for the electrodes with low sulfur loading and 7–9 μL mg^{-1} for high sulfur loading electrodes. LAND CT2100A (5 V, 10 mA, Wuhan LANHE) was served to carry out the galvanostatic discharge and charge tests in a potential range of 1.7–2.8 V versus Li/Li^+. The specific capacities were calculated based on the mass of sulfur on each electrode. CV curves, EIS tests (100 kHz~0.01 Hz) were operated by electrochemical workstation (Gamry Interface 1000, Germany). The Li^+ diffusion coefficients are respectively calculated based on the CV and EIS results, using the Eqs. (S7) and (S8). According to the Nyquist plots in Figs. 4, S20 and S21a-b, the Warburg factors can be obtained based on the relationship between $w^{-1/2}$ and Z′, the corresponding raw data and fitting lines are shown in Fig. S21c-f.

2.10. Computational methods

All calculations were carried out using the density functional theory (DFT) as implemented in the Vienna Ab initio Simulation Package (VASP). The projector augmented wave (PAW) potentials and generalized gradient approximation (GGA) of the Perdew-Burke-Ernzerhof (PBE) functional were used for the electron-ion interaction and exchange-correlation energy, respectively. To study the adsorption behaviors of Li_2S_x (Li_2S and Li_2S_6), five-layer slabs with the 5 × 5 × 1 and 4 × 4 × 1 supercells were built for MoN and Mo_2N surfaces, respectively, where the bottom two-layers were fixed, and the remaining atoms were fully relaxed until the force on each atom was less than 0.01 eV $Å^{-1}$. The cutoff energy for the plane wave expansion was set to 500 eV. The Brillouin zone was sampled by Γ-centered 3 × 3 × 1 k-point mesh. The vacuum layer of 15 Å in the z direction was chosen to eliminate the interactions between the periodic images. The absorption energies (E_{ads}) of Li_2S_x on the substrates were calculated as follows:

$$E_{ads} = E_{all} - E_{Li_2S_x} - E_{sub}$$

where E_{all}, $E_{Li_2S_x}$ and E_{sub} represent the total energies of the absorbed systems, isolated Li_2S_x clusters and substrates, respectively.

3. Results and discussion

Fig. 1a shows the typical preparation process of RGB-MN and LGB-MN. Firstly, MoO_2 hollow microspheres were prepared by the hydrothermal treatment of the mixture of molybdenyl acetylacetonate, n-butyl alcohol, and HNO_3. The formed MoO_2 hollow spheres with the size of 400–600 nm are composed of the primary nanoparticles (NPs) with a size of 20–30 nm and the crystal structure can be indexed to the monoclinic MoO_2 (JCPDS No. 32–0671) (Figs. S1 and S2). After the nitridation in NH_3 atmosphere at 720 °C, the hollow microsphere structure was retained according to the scanning electron microscopy (SEM) and transmission electron microscopy (TEM) images shown in Fig. 1b and the inset, and numerous small NPs can be observed on the outer surface. In Fig. 1c and the inset, the high magnification TEM images show the formation of many MoN GBs, Mo_2N GBs and phase boundaries between Mo_2N and MoN (marked by yellow lines), which can be confirmed by the lattice spacings of 0.28, 0.24 and 0.208 nm corresponding to the MoN (002), Mo_2N (111) and (200) planes, respectively. The X-ray diffraction (XRD) pattern (Fig. 1f) further confirms the formation of hexagonal structure MoN (JCPDS No. 25–1367) and cubic structure Mo_2N (JCPDS No. 25–1366) in such hollow microspheres. When the nitridation temperature increased to 820 °C, the SEM image in Fig. 1d shows the NPs on the sphere surface become much larger, and the inset TEM image shows the hollow structure is still retained but with a much thicker wall. However, the TEM image in Fig. 1e shows the GBs become much fewer due to the formation of larger grains. The inset TEM image in Fig. 1e and the XRD pattern in Fig. 1f show these grains can be indexed to the cubic structure Mo_2N (JCPDS No. 25–1366). The TEM results qualitatively show that RGB-MN has smaller grain sizes and more GBs, compared to LGB-MN. The full width at half maximum (FWHM) of the XRD peaks of RGB-MN is much larger than that of LGB-MN, and the calculated average grain size based on the Scherrer equation (Eq. (S1)) of RGB-MN is around 8.16 nm, which is much smaller than that of LGB-MN (16.37 nm). The calculation details can be found in Table S1. The calculated smaller grain size in RGB-MN can qualitatively indicate a higher density of GBs [29,30]. The decrease of GB density in LGB-MN should be ascribed to the formation of larger pure Mo_2N grains. With a low temperature nitridation, the replacement of O by N in the crystalline structure of MoO_2 occurs, which leads to defects in bulk, generating many tiny crystals and thus, more GBs. However, when the temperature increases above 750 °C, the Mo in MoN will be further reduced to $Mo^{\delta+}$ (δ < 4) to form Mo_2N, and the formed small grains tend to grow larger to reduce their total surface energy [10,16,21]. The differences between the surface morphology of RGB-MN and LGB-MN are caused by the different sizes of primary particles (Fig. 1b and d). The primary particles in LGB-MN are bigger than that of RGB-MN due to the higher nitridation temperature, which leads to a larger grain size and the formation of smoother surface. Energy dispersive spectrometer (EDS) elemental mappings in Fig. S3 show the homogenous distribution of Mo and N elements in them. It should be noted that such a porous hollow microsphere structure ensures the high accessibility and high utilization of GBs during the LiPS adsorption and deposition.

In order to exclude the effects of insufficient nitridation products of Mo_2N on the above performance improvement, density functional theory (DFT) calculations were firstly performed to comparatively investigate the adsorption energy (E_{ads}) of LiPSs on different MoN and Mo_2N surfaces based on the TEM images in Fig. 1b-e. Fig. S5 shows the optimized structures and the corresponding adsorption energy of Li_2S_6 on the MoN (002) is −9.92 eV, and for the Mo_2N (200), (111) and (220) surfaces, the adsorption energies are −7.40, −9.14 and −9.76 eV, respectively. These results suggest the RGB-MN and LGB-MN should have similar anchoring ability towards LiPSs. Besides, no obvious difference in adsorption energies of Li_2S on MoN and Mo_2N surfaces is observed. To investigate the adsorption ability of RGB-MN and LGB-MN towards LiPSs, visualized adsorption experiments were conducted. As

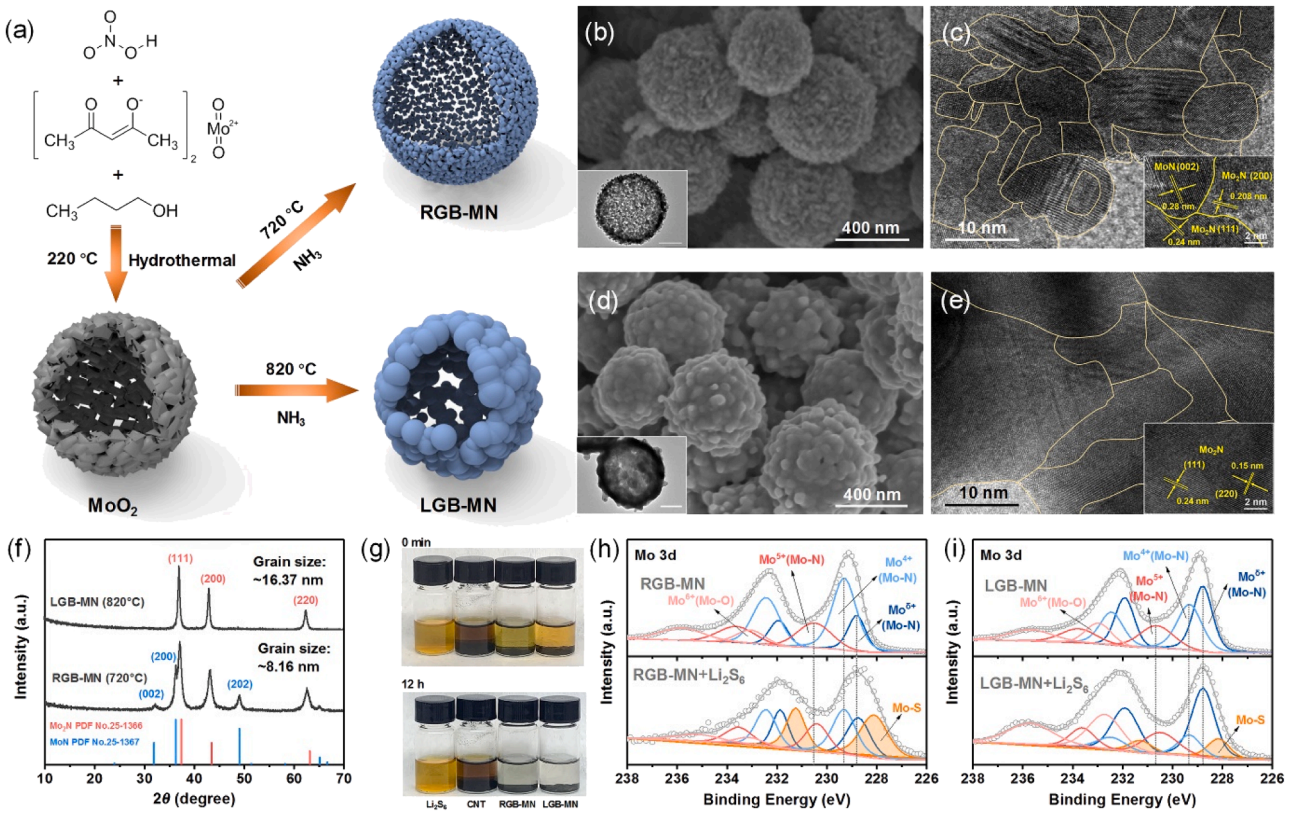

Fig. 1. (a) Schematic illustration of the fabrication process of RGB-MN and LGB-MN. (b) and (d) SEM and TEM (inset, the scale bar is 200 nm) images of RGB-MN and LGB-MN. (c) and (e) TEM images of RGB-MN and LGB-MN with the GBs marked by the lines, and the insets in them show the lattice spacings of the grains. (f) XRD patterns of LGB-MN and RGB-MN. (g) Photographs of Li_2S_6 solution and the Li_2S_6 solutions with carbon nanotube (CNT), RGB-MN and LGB-MN just added and after 12 h. Mo 3d XPS spectra of (h) RGB-MN and (i) LGB-MN before and after Li_2S_6 adsorption.

shown in Fig. 1g, the Li_2S_6 solutions (2 mM Li_2S_6 in dioxolane/dimethoxyethane (DOL/DME) mixture) with RGB-MN and LGB-MN become almost colorless after 12 h and show no apparent differences, suggesting their strong adsorption ability towards LiPSs. Note that the color of Li_2S_6 solution quickly became much lighter once the RGB-MN was added, meaning it can adsorb the LiPSs rapidly, which is important to suppress the shuttling of LiPSs and realize their fast conversion. Considering the difference between the specific surface areas of LGB-MN and RGB-MN (Fig. S6 and Table S2), 20 mg RGB-MN and 40 mg LGB-MN with identical surface areas were also used to measure the adsorption ability to Li_2S_6 (Fig. S7). After 0.5 h, the solution with RGB-MN became colorless, but the solution with LGB-MN still showed light yellow color. After a 12 h adsorption, both of these two solutions became colorless, which further proves the strong adsorption ability of them to LiPSs but the fast adsorption rate with RGB-MN. And, according to previous reports, the dislocations at the GBs can alter the binding energies towards the reactants [31,32], which enhances the adsorption rate. Thus, it can be speculated the density of GBs should be the main factor affecting the performance of RGB-MN and LGB-MN in suppressing the shuttling and enhancing the reaction kinetics of LiPSs.

The surface chemistry of RGB-MN and LGB-MN before and after Li_2S_6 adsorption was further investigated by X-ray photoelectron spectroscopy (XPS). As shown in Fig. 1h and i, after the Li_2S_6 adsorption, the Mo-S bond can be found at ~ 228.11 and 231.24 eV, which can be elucidated by the polarization of electrons transferring from the terminal sulfur atoms in Li_2S_6 (S_T^{-1}) to the electropositive molybdenum [33]. It can be found that the content of Mo-S in RGB-MN after adsorption is higher than that of LGB-MN, which indicates that RGB-MN with more GBs has stronger interaction with LiPSs. Moreover, the content of Mo^{4+} (~229.31 eV) became lower, and the content of $Mo^{\delta+}$ (~228.80 eV) became higher in both RGB-MN (Mo^{4+}: from 47% to 27%; $Mo^{\delta+}$: from 18% to 21%) and LGB-MN (Mo^{4+}: from 31% to 11%; $Mo^{\delta+}$: from 34% to 36%) after Li_2S_6 adsorption. The increase of Mo cations with lower valences suggests they should have a strong ability to obtain electrons from LiPSs. These results suggest that RGB-MN and LGB-MN have the same adsorption mechanism towards LiPSs, but the rich GBs could enhance the adsorption ability by the formation of more Mo-S bonds proved by the much larger peak area (Fig. 1i) [34].

To verify the effect of GBs on the redox reaction kinetics of LiPSs, the symmetric cells were assembled using a 0.2 M Li_2S_6 as the electrolyte and the above samples loaded on the carbon paper as the electrodes. As shown in Fig. 2a, the higher current density and smaller peak separation of the cell with the RGB-MN electrode suggest better redox kinetics and reversibility of LiPSs conversion. The symmetric cell of RGB-MN also shows a higher current density at a scan rate at 50 mV s^{-1} compared with LGB-MN. (Fig. S8), which also indicates the enhanced LiPS conversion kinetics on GBs-enriched catalysts. To further investigate the GBs mediated LiPSs deposition behavior, Li_2S nucleation tests were carried out with the Li_2S_8 as the initial active material. As shown in Fig. 2b, c, according to the sigmoidal cumulative distribution function follows the Avrami form [35], the cell with RGB-MN electrode exhibits a specific Li_2S deposition capacity of 473.1 mAh g^{-1} (the area marked by light blue), much higher than the cells with LGB-MN (325.5 mAh g^{-1}) and CNT (340 mAh g^{-1}, Fig. S9) electrodes. Besides, the deposition peak of the cell with the RGB-MN electrode appears much earlier (2201 s) than that of LGB-MN (11,987 s) and shows the highest current intensity, suggesting fast LiPS trapping and Li_2S nucleation. Note that the CNT with high conductivity and SSA shows fast nucleation rate compared to that of LGB-MN, which further suggests the high quantity of GBs is critical to improving the reaction kinetics by serving as active sites for deposition. This speculation was further confirmed by the analysis of Li_2S nucleation and growth models on different surfaces.[36–38] The

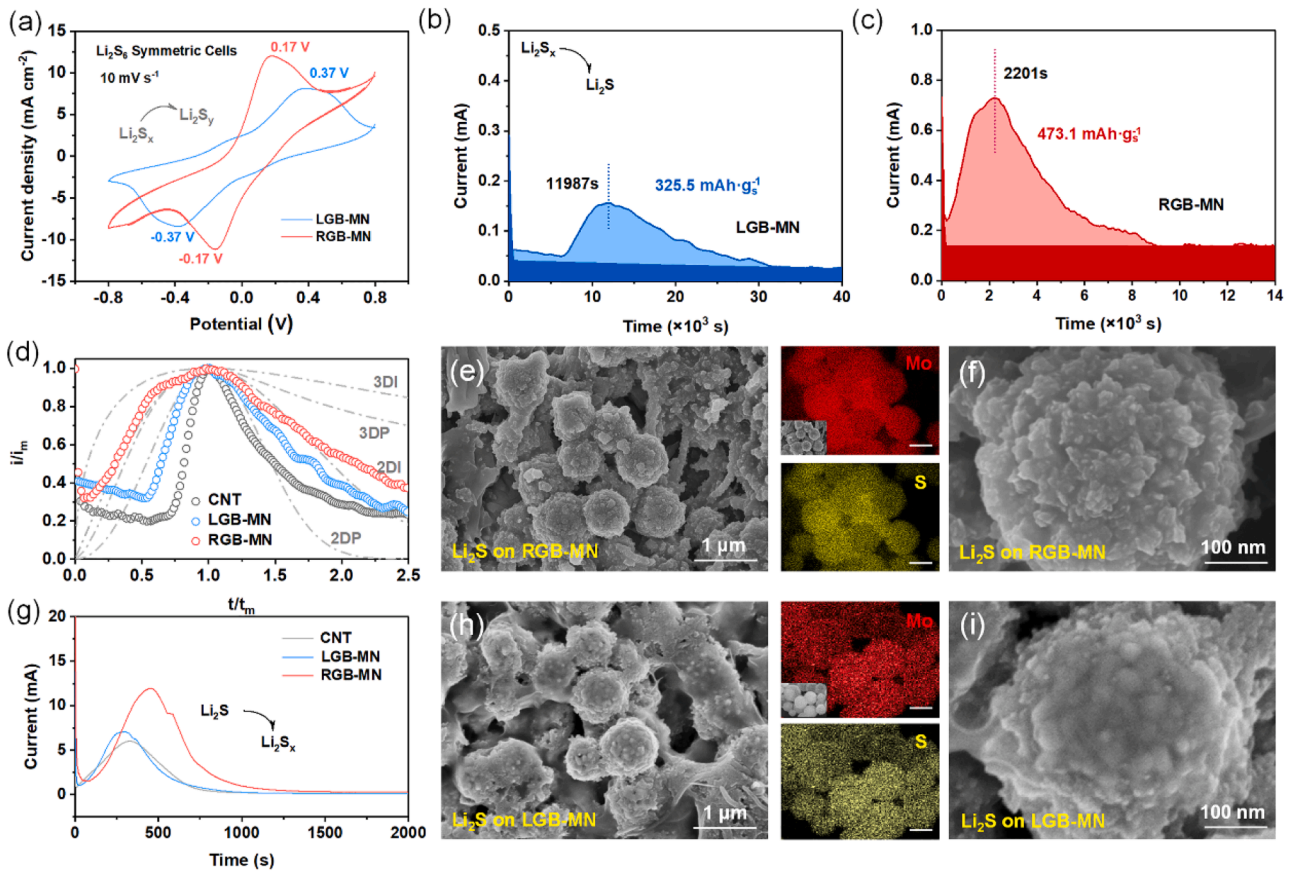

Fig. 2. (a) CV curves of Li_2S_6-symmetric cells with different catalysts. (b) and (c) Potentiostatic discharge profiles at 2.08 V. (d) Dimensionless transient (symbols) corresponded to Fig. 2b and c in comparison with theoretical 2D and 3D models. Low magnification SEM images of (e-f) RGB-MN and (h-i) LGB-MN after Li_2S deposition at 2.08 V and the corresponding EDS mappings of Mo and S. Scale bar: 500 nm (g) Potentiostatic charge profiles at 2.40 V.

current–time transient profiles (Fig. 2d) are obtained from the Li_2S nucleation curves in Fig. 2b-c and compared with the theoretical two-dimensional (2D) and three-dimensional (3D) nucleation and growth models (dot-dash lines, based on the Eqs. (S2)-(S5)) [39]. i_m and t_m are the peak current and the time required to achieve the peak current. The 2D progressive nucleation (2DP) and 2D instantaneous (2DI) nucleation are followed by the incorporation of adatoms into the lattice interface, and the 3D progressive (3DP) nucleation and 3D instantaneous (3DI) nucleation are followed by a volume diffusional controlled growth [11,39]. According to Fig. 2d, it can be found that LGB-MN exhibits a higher instantaneous deposition tendency compared with CNT, although both of them follow 2D nucleation model, which suggests the more rapid formation of Li_2S nuclei on LGB-MN due to the GBs as nucleation hot spots. In contrast, CNT with low LiPSs affinity reveals a progressive deposition behavior, leading to the slow accumulation of solid Li_2S on CNT surface and limited utilization of the inner space (Fig. S10). On the RGB-MN surface, the Li_2S nucleation and growth follow the hybrid models of 2DI and 3DP, which also means the rapid formation of Li_2S nuclei, but the fast charge transfer and efficient LiPSs immobilization around the GBs lead to the 3D directional Li_2S precipitation.

The Li_2S morphology after the deposition was characterized by SEM and EDS. As shown in Fig. 2e and f, the Li_2S is mainly deposited on the RGB-MN surface, forming a thick and undulation coating by the 3D aggregation of sheet-like Li_2S. In contrast, as shown in Fig. 2h and i, the Li_2S deposited on LGB-MN shows a thin coating layer morphology, which passivates the catalyst surface for the following LiPS adsorption and Li_2S formation. These results agree well with the aforementioned growth model. Lateral growth rates ($N_0k_g^2$, N_0 represents the density of available nucleation site, k_g is the nucleus lateral growth-rate constant) of Li_2S on LGB-MN and RGB-MN were calculated based on the BFT (A. Beweick, M. Fleischman, and H.R. Thirsk) model (Eq. (S6)), and the values are 1.44×10^{-12} mol^2 cm^{-6} s^{-2} for LGB-MN and 4.28×10^{-11} mol^2 cm^{-6} s^{-2} for RGB-MN. The oxidation of the deposited Li_2S was also conducted by a potentiostatic charge process at 2.4 V after two-stage galvanostatic discharge processes to 1.8 V [28,40]. As shown in Fig. 2g, the cell with RGB-MN shows a much larger oxidation current density than those with LGB-MN and pure CNT electrode due to a large amount of Li_2S deposited on its surface and a better oxidation kinetics. However, the largest amount of Li_2S deposits also passivates the surface of RGB-MN, leading to a longer time for RGB-MN to reach the fastest dissolution kinetics. According to the above results, we can conclude that for RGB-MN, as shown in Fig. 3a, the abundant GBs provide large numbers of Li_2S adsorption and nucleation sites, which mediate the Li_2S growth around the GBs and avoid the formation of a dense Li_2S layer to passivate the electrode surface, leaving sufficient channels to ensure the continuous LiPSs diffusion and the subsequent Li_2S deposition. However, on the LGB-MN surface (Fig. 3b), the uniformly deposited Li_2S at the beginning easily passivates the catalyst surface, hindering the subsequent LiPSs conversion and Li_2S deposition.

To investigate the practical uses of LGB-MN and RGB-MN in Li-S batteries, we prepared the hybrid interlayers on the PP separator by mixing them with CNT together, and they are denoted as LGB-MN/CNT and RGB-MN/CNT. The prepared interlayers have similar areal mass loading around 0.4 mg cm^{-2} and a thickness of about 10 μm according to the cross-sectional SEM image in Fig. 11a. The corresponding elemental mappings indicate the uniform distribution of Mo, N and C elements (Fig. S11b-c). The photo of RGB-MN/CNT modified separator in the insets of Fig. S11a reveals the good flexibility and strong adherence of the interlayer. The 2032 coin cells were assembled using Super

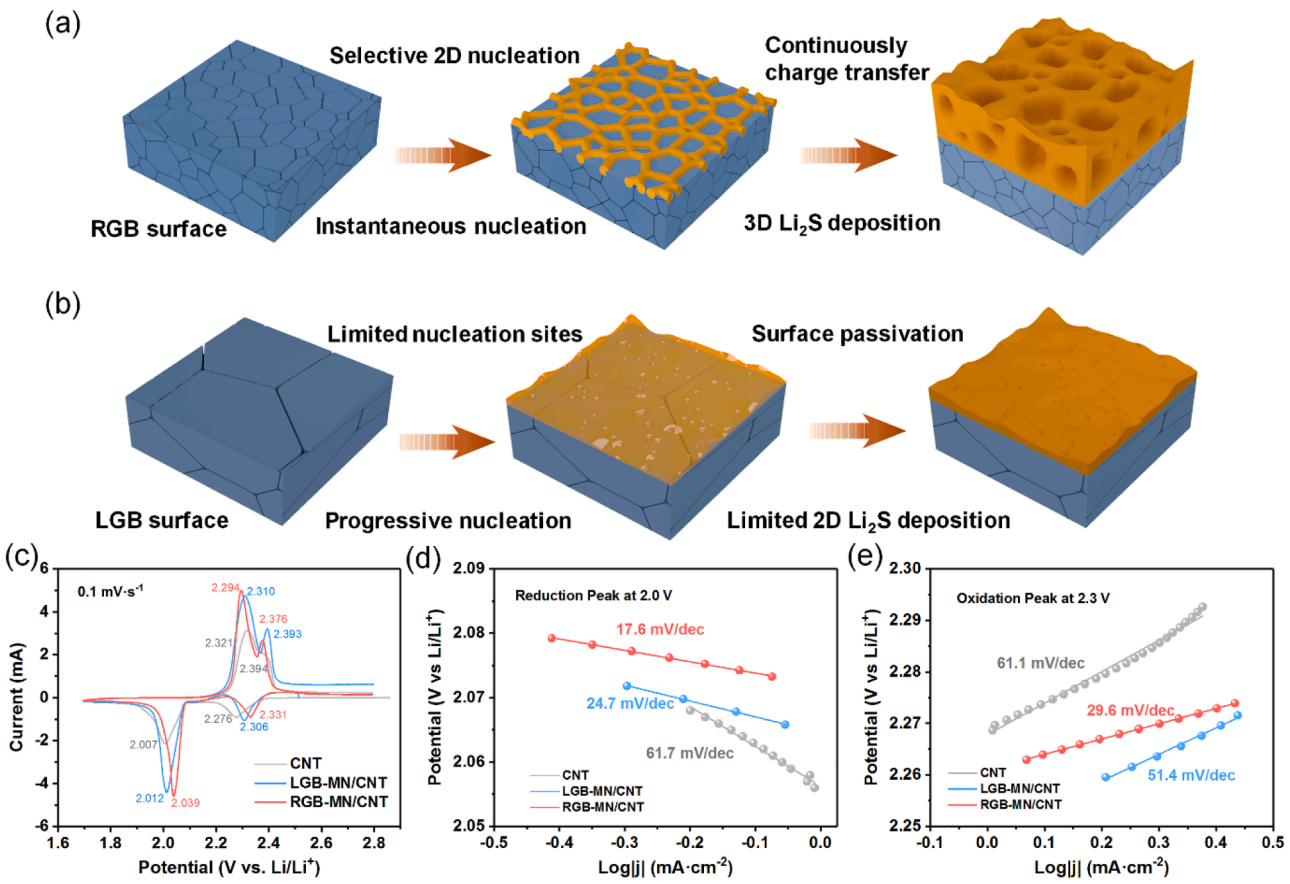

Fig. 3. (a) and (b) Schematic illustration of the regulated Li_2S nucleation and deposition process by GBs. (c) CV curves of the Li-S batteries with different interlayers. The Tafel plots of the (d) conversion from LiPSs to Li_2S according to the reduction peak at 2.0 V, and (e) the conversion from Li_2S to LiPSs according to the oxidation peak at 2.3 V in CV test.

P/sulfur hybrid (sulfur loading around 75 wt%, Fig. S12) as the cathode, Li foil as the anode and the modified separators, and the cyclic voltammetry tests were carried out in a voltage range of 1.7–2.8 V at a scan rate of 0.1 mV s^{-1}. In Fig. 3c, the reduction peaks at around 2.3 and 2.0 V represent the conversion from S_8 to LiPSs and then to Li_2S, and the oxidation peaks around 2.3 and 2.4 V are derived from the conversion of Li_2S to LiPSs and then to S_8 [41,42]. It is shown the cathodic peaks shift to a higher potential and the anodic peaks shift to a lower potential for the battery with RGB-MN/CNT interlayer, compared with that with LGB-MN/CNT or pure CNT interlayers, suggesting the lower electrochemical polarization and enhanced redox conversion between LiPSs and Li_2S/sulfur. To further prove the enhanced reaction kinetics, the Tafel plots based on the two reduction peaks and oxidation peak at 2.3 V are calculated. In Fig. S13 the Tafel slopes of the batteries with RGB-MN, LGB-MN and pure CNT interlayers are 14.7, 34.9 and 89.9 mV dec^{-1} for the reduction process from S_8 to LiPSs (peaks at 2.3 V), respectively. As shown in Fig. 3d and e, for the conversion from LiPSs to Li_2S (peaks at 2.0 V), the values are calculated to be 17.6, 24.7 and 61.7 mV dec^{-1}. Meanwhile, for the oxidation process, the Tafel slopes are 29.6, 51.4 and 61.7 mV dec^{-1}. Note that the battery with RGB-MN/CNT interlayer shows the lowest Tafel slopes among three samples, and the Tafel slopes are also lower than some catalysts reported by previous reports (Table S3), which indicates the enhanced redox kinetics with the help of RGB-MN. The CV curves with different scanning rates are shown in Fig. S14, based on the Randles-Sevick equation (Eq. (S7)), the battery with RGB-MN/CNT interlayer shows a much higher Li^+ diffusion coefficient than the other two batteries in both reduction and oxidation process, further suggesting the enhanced redox kinetics (Table S4).

The electrochemical performance of the batteries with different interlayers was further investigated. The capacity contribution of RGB-MN in the battery is negligible compared with the sulfur in the assembled battery (Fig. S15). Galvanostatic discharge-charge tests were conducted in a voltage range from 1.7 to 2.8 V at different current densities. As shown in Fig. 4a, the battery with RGB-MN/CNT interlayer delivers discharge capacities of 1350 and 698 mAh g^{-1} at 0.2 and 4 C, respectively, and when the current density backed to 0.5 C, a capacity of 980 mAh g^{-1} can still be restored. The corresponding galvanostatic discharge-charge curves in Fig. 4b also exhibit two obvious discharge voltage plateaus even under the high current densities, further suggesting the enhanced reaction kinetics. In contrast, the batteries with LGB-MN/CNT and CNT interlayers only exhibit the capacities of 541 and 287 mAh g^{-1} at 4 C. The battery with CNT interlayer shows the highest polarization, which should be ascribed to slow conversion kinetics of LiPSs due to the nonpolar surface and poor catalytic activity of CNT. Meanwhile, the polarization overpotentials at various current densities, and the positive charge potential peaks at 0.2 C are also much smaller for the battery with RGB-MN/CNT interlayer (Fig. 4c and Figs. S16 and S17). Due to the 3D morphology of Li_2S on RGB-MN, the infiltration of the electrolyte can be easily achieved, providing abundant Li^+ diffusion channels. At the same time, more GBs on the surface can provide more Li^+ pathways and active sites to accelerate the Li_2S dissociation. Thus, the battery with RGB-MN/CNT interlayers showed decreased overpotential for Li_2S oxidation in the following cycles [43–45].

The cyclic performances of the battery with different interlayers are shown in Figs. 4d and S18. The initial discharge capacity of the battery with RGB-MN/CNT interlayer at 0.5 C is around 1120 mAh g^{-1}, and after 300 cycles, a discharge capacity of 730 mAh g^{-1} could be maintained, showing a very low capacity decay of 0.116% per cycle under

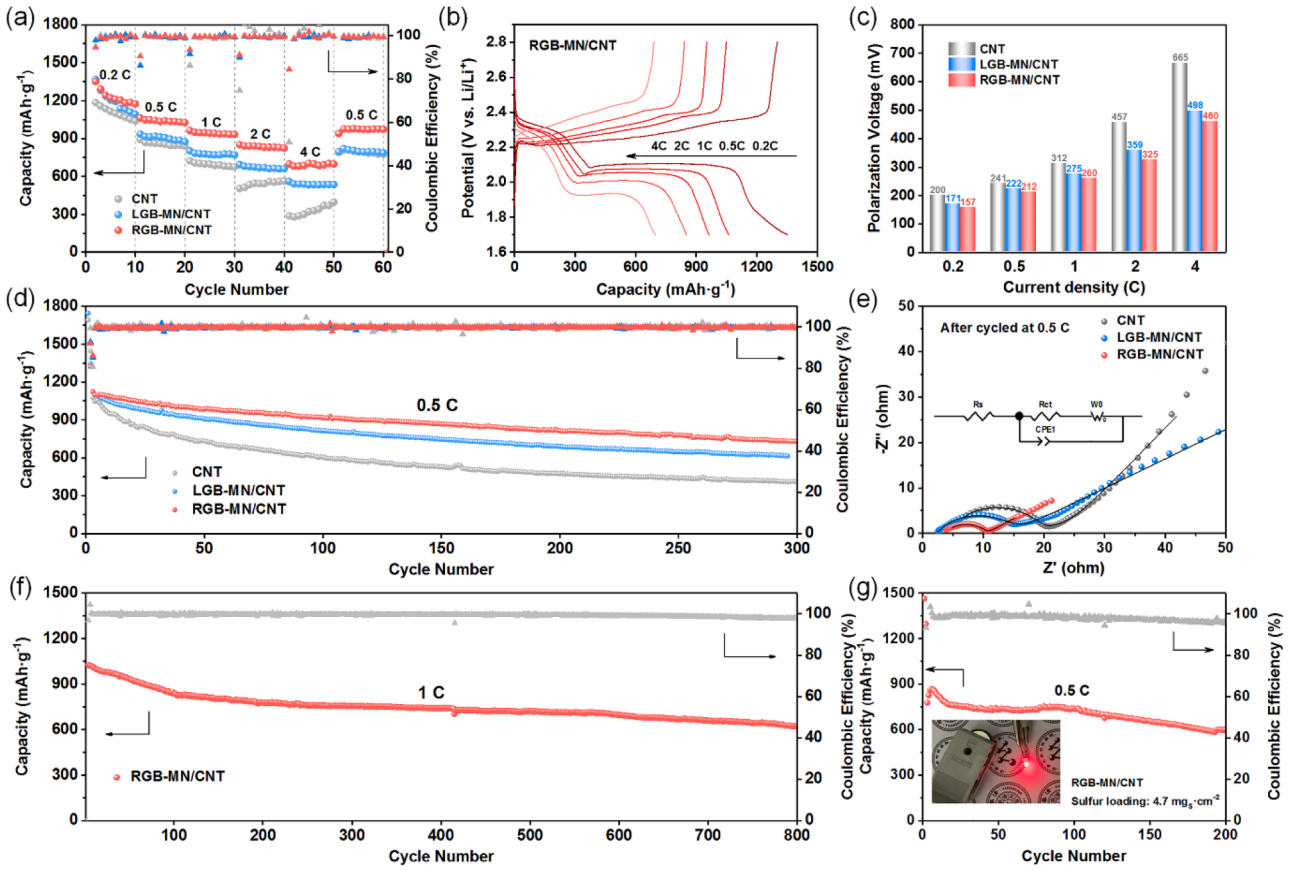

Fig. 4. (a) The rate capability of Li-S battery with different interlayers. (b) Charge and discharge profiles of the battery with RGB-MN/CNT interlayer at different current densities. (c) The values of polarization voltage of the above batteries. (d) Cycling performance of Li-S battery with different interlayers at 0.5 C. (e) Electrochemical impedance spectra (EIS) and fitting results of Li-S batteries with different interlayers after 0.5 C cycling. Inset is the equivalent circuit used for Nyquist plots fitting. (f) Long cycling performance of battery with RGB-MN/CNT interlayer under 1 C, and (g) Cycling performance at 0.5 C with a high areal sulfur loading of 4.7 mg cm^{-2}. Inset is the LED powered by the battery after 200 cycles.

such low current density. But for the batteries with LGB-MN/CNT and CNT interlayers, the discharge capacities were only 614 and 407 mAh g^{-1} after 300 cycles, showing the capacity decays of 0.15% and 0.24% per cycle, respectively. These results suggest that the RGB-MN/CNT interlayer could effectively suppress the LiPSs shuttling and improve sulfur utilization. Moreover, the morphology of the RGB-MN/CNT interlayer after cycling at 0.5 C was also characterized (Fig. S19). The RGB-MN shows intimate contact with CNT on the interlayer. The spherical morphology of RGB-MN with many NPs is well retained, which suggests the high structural stability of the RGB-MN catalyst with less degradation, and therefore contributes to the stable cycling performance. To further confirm the promoted redox reaction kinetics, the Nyquist plots of the assembled batteries with different interlayers after cycling were fitted by an equivalent circuit. As shown in Fig. 4e, after 300 cycles at 0.5 C, the batteries with RGB-MN/CNT show the semicircle with a much smaller diameter (R_{ct}) than the other two batteries, suggesting the enhanced LiPS conversion kinetics by RGB-MN, which avoids the aggregation and accumulation of Li_2S in the interlayers. However, because of weak catalytic activity and the regulation ability of LGB-MN/CNT and CNT towards Li_2S deposition, the non-uniform deposition of Li_2S in the interlayers leads to the increase of ion diffusion and electron transfer resistances after cycling. The fitted details are listed in the Supporting Information (inset of Figs. 4e, S20 and S21 and Tables S5 and S6). The Li^+ diffusion coefficients of the cells with different interlayers before and after cycling were also calculated based on the EIS results and Eq. (S8). The battery with RGB-MN/CNT exhibits higher Li^+ diffusion coefficients values before and after cycling, indicating the faster mass transfer. The RGB-MN/CNT also shows lower R_{ct} values with slight change after different cycles, which indicates the fast charge transfer and the stable catalytic activity of RGN-MN on the redox interfaces during the redox process. The influences of the interlayer thickness on the battery performance were also investigated. As shown in Figs. S22 and S23, the batteries with too thick (*e. g.* 20 μm) or too thin (*e. g.* 5 μm) interlayers show inferior cycling stability, possibly because the thick layer hinders the ion diffusion, and the thin layer cannot effectively block the LiPS shuttling.

The long cycling stability of the battery with the RGB-MN/CNT interlayer was further evaluated at 1 C (Fig. 4f). The initial discharge capacity of 1025 mAh g^{-1} can be obtained, and after 800 cycles, a discharge capacity of 622.5 mAh g^{-1} still retained, suggesting a low capacity fading rate of around 0.049% per cycle, which is much lower than the other interlayers recently reported (Table S7). To further prove its potential for commercialized applications, the cycling stability of the battery with higher areal sulfur loading of 4.7 mg cm^{-2} was also investigated. When cycled at 0.2 C (Fig. S24), an initial discharge capacity of 900 mAh g^{-1} can be achieved, showing high capacity retention of 87.6% after 100 cycles. For longer cycling at 0.5 C, as shown in Fig. 4g, the battery with high sulfur loading shows an activation process in the initial cycles, a relatively high capacity of 600 mAh g^{-1} can be maintained after 200 cycles, suggesting the capacity retention of 77.2%. Note that such a battery after 200 cycles still can power a light-emitting diode (LED) overnight. The batteries with a lower E/S ratio of 5 μL mg^{-1} were also assembled (Fig. S25). It is shown that high capacities over 900 mAh g^{-1} and 700 mAh g^{-1} can be achieved with the areal sulfur loading around 5.1 and 8.3 mg cm^{-2}, respectively. High capacity retention can also be obtained after 100 cycles (62% for 5.1 mg cm^{-2}), and the

discharge-charge profiles show small polarization as shown in Fig. S25b, indicating a great potential of the interlayer with RGB-MN catalyst in promoting the application of Li-S batteries. The performance comparison of the Li-S batteries with RBG-MN under high areal sulfur loading and other reported Li-S batteries is listed in Table S8.

4. Conclusions

In summary, the hollow microspheres composed of MoN-Mo_2N heterostructure with abundant GBs were prepared and used as the models to reveal the functions of GBs in guiding the 3D deposition and growth of Li_2S. The GBs acting as the 2D nucleation sites not only show strong and fast adsorption ability towards LiPSs but also guide the Li_2S deposition around them, effectively avoiding the catalyst surface passivation. As a result, such hollow microspheres lead to a high capacity Li_2S deposition and greatly enhances the conversion kinetics of LiPSs. The assembled battery with the interlayer composed of the above microspheres and CNT showed a low capacity decay of 0.049% per cycle at 1 C for 800 cycles and a high capacity of 698 mAh g^{-1} at 4 C. Even with high sulfur loading of 4.7 mg cm^{-2}, a relatively high capacity of 600 mAh g^{-1} and capacity retention of 77.2% can be maintained after 200 cycles under 0.5 C, showing the great potential to suppress the shuttling of LiPSs. Overall, this work shows a new direction of designing the high-performance catalysts for Li-S batteries, which can also be used to tune the properties of catalysts for different applications.

CRediT authorship contribution statement

Jin-Lin Yang: Conceptualization, Investigation, Formal analysis, Writing – original draft. **Da-Qian Cai:** Data curation, Writing – original draft. **Qiaowei Lin:** Formal analysis, Writing – review & editing. **Xin-Yu Wang:** Data curation. **Zou-Qiang Fang:** Methodology. **Ling Huang:** Formal analysis. **Zhi-Jie Wang:** Software, Investigation, Methodology. **Xiao-Ge Hao:** Data curation, Investigation. **Shi-Xi Zhao:** Project administration, Writing – review & editing, Supervision. **Jia Li:** Software, Supervision. **Guozhong Cao:** Writing – review & editing, Supervision. **Wei Lv:** Project administration, Writing – review & editing, Supervision.

Declaration of Competing Interest

The authors declare that they have no known competing financial interests or personal relationships that could have appeared to influence the work reported in this paper.

Acknowledgments

This work was supported by National Natural Science Foundation of China (No. 51772164, 52022041 and 11874036), National Key Research and Development Program of China (2018YFE0124500), Local Innovative and Research Teams Project of Guangdong Pearl River Talents Program (Grant No. 2017BT01N111), and Shenzhen Basic Research Project (JCYJ20190813172807127 and JCYJ20180508152037520).

Appendix A. Supporting information

Supplementary data associated with this article can be found in the online version at doi:10.1016/j.nanoen.2021.106669.

References

[1] J. Wang, Y.S. He, J. Yang, Sulfur-based composite cathode materials for high-energy rechargeable lithium batteries, Adv. Mater. 27 (2015) 569–575.
[2] Z.W. Seh, Y. Sun, Q. Zhang, Y. Cui, Designing high-energy lithium-sulfur batteries, Chem. Soc. Rev. 45 (2016) 5605–5634.
[3] X. Chen, T. Hou, K.A. Persson, Q. Zhang, Combining theory and experiment in lithium–sulfur batteries: current progress and future perspectives, Mater. Today 22 (2019) 142–158.
[4] D. Liu, C. Zhang, G. Zhou, W. Lv, G. Ling, L. Zhi, Q.H. Yang, Catalytic effects in lithium-sulfur batteries: promoted sulfur transformation and reduced shuttle effect, Adv. Sci. 5 (2018), 1700270.
[5] Z.-W. Zhang, H.-J. Peng, M. Zhao, J.-Q. Huang, Heterogeneous/homogeneous mediators for high-energy-density lithium-sulfur batteries: progress and prospects, Adv. Funct. Mater. 28 (2018), 1707536.
[6] H.J. Peng, G. Zhang, X. Chen, Z.W. Zhang, W.T. Xu, J.Q. Huang, Q. Zhang, Enhanced electrochemical kinetics on conductive polar mediators for lithium-sulfur batteries, Angew. Chem. Int. Ed. 55 (2016) 12990–12995.
[7] L. Ma, R. Chen, G. Zhu, Y. Hu, Y. Wang, T. Chen, J. Liu, Z. Jin, Cerium oxide nanocrystal embedded bimodal micromesoporous nitrogen-rich carbon nanospheres as effective sulfur host for lithium-sulfur batteries, ACS Nano 11 (2017) 7274–7283.
[8] C. Ye, L. Zhang, C. Guo, D. Li, A. Vasileff, H. Wang, S.-Z. Qiao, A 3D hybrid of chemically coupled nickel sulfide and hollow carbon spheres for high performance lithium–sulfur batteries, Adv. Funct. Mater. 27 (2017), 1702524.
[9] T. Zhou, W. Lv, J. Li, G. Zhou, Y. Zhao, S. Fan, B. Liu, B. Li, F. Kang, Q.-H. Yang, Twinborn TiO2–TiN heterostructures enabling smooth trapping–diffusion–conversion of polysulfides towards ultralong life lithium–sulfur batteries, Energy Environ. Sci. 10 (2017) 1694–1703.
[10] J.-L. Yang, S.-X. Zhao, Y.-M. Lu, X.-T. Zeng, W. Lv, G.-Z. Cao, Clinical characteristics and risk assessment of newborns born to mothers with COVID-19, Nano Energy 68 (2020), 104356.
[11] M. Zhao, H.J. Peng, J.Y. Wei, J.Q. Huang, B.Q. Li, H. Yuan, Q. Zhang, Small Methods (2019), 1900344.
[12] C. Zhao, G.-L. Xu, Z. Yu, L. Zhang, I. Hwang, Y.-X. Mo, Y. Ren, L. Cheng, C.-J. Sun, Y. Ren, X. Zuo, J.-T. Li, S.-G. Sun, K. Amine, T. Zhao, A high-energy and long-cycling lithium–sulfur pouch cell via a macroporous catalytic cathode with double-end binding sites, Nat. Nanotechnol. 16 (2020) 166–173.
[13] J. Xie, Y.W. Song, B.Q. Li, H.J. Peng, J.Q. Huang, Q. Zhang, Direct intermediate regulation enabled by sulfur containers in working lithium-sulfur batteries, Angew. Chem. Int. Ed. 59 (2020) 22150–22155.
[14] S. Najmaei, Z. Liu, W. Zhou, X. Zou, G. Shi, S. Lei, B.I. Yakobson, J.-C. Idrobo, P. M. Ajayan, J. Lou, Vapour phase growth and grain boundary structure of molybdenum disulphide atomic layers, Nat. Mater. 12 (2013) 754–759.
[15] C.W. Li, J. Ciston, M.W. Kanan, Electroreduction of carbon monoxide to liquid fuel on oxide-derived nanocrystalline copper, Nature 508 (2014) 504–507.
[16] X. Feng, K. Jiang, S. Fan, M.W. Kanan, Grain-boundary-dependent CO_2 electroreduction activity, J. Am. Chem. Soc. 137 (2015) 4606–4609.
[17] Z. Chen, T. Wang, B. Liu, D. Cheng, C. Hu, G. Zhang, W. Zhu, H. Wang, Z.-J. Zhao, J. Gong, Grain-boundary-rich copper for efficient solar-driven electrochemical CO_2 reduction to ethylene and ethanol, J. Am. Chem. Soc. 142 (2020) 6878–6883.
[18] S. Liu, J. Xiao, X.F. Lu, J. Wang, X. Wang, X.W. Lou, Efficient electrochemical reduction of CO_2 to HCOOH over Sub-2nm SnO2 quantum wires with exposed grain boundaries, Angew. Chem. Int. Ed. 58 (2019) 8499–8503.
[19] A. Magasinski, P. Dixon, B. Hertzberg, A. Kvit, J. Ayala, G. Yushin, High-performance lithium-ion anodes using a hierarchical bottom-up approach, Nat. Mater. 9 (2010) 353–358.
[20] M.M. Rahman, J.-Z. Wang, M.F. Hassan, D. Wexler, H.K. Liu, Amorphous carbon coated high grain boundary density dual phase Li4Ti5O12-TiO2: a nanocomposite anode material for Li-ion batteries, Adv. Energy Mater. 1 (2011) 212–220.
[21] C. Wang, S. Wang, Y.-B. He, L. Tang, C. Han, C. Yang, M. Wagemaker, B. Li, Q.-H. Yang, J.-K. Kim, F. Kang, Combining fast Li-ion battery cycling with large volumetric energy density: grain boundary induced high electronic and ionic conductivity in Li4Ti5O12 spheres of densely packed nanocrystallites, Chem. Mater. 27 (2015) 5647–5656.
[22] K. Dewangan, S.S. Patil, D.S. Joag, M.A. More, N.S. Gajbhiye, Topotactical nitridation of α-MoO3 fibers to γ-Mo2N fibers and its field emission properties, J. Phys. Chem. C 114 (2010) 14710–14715.
[23] D. Tian, X. Song, M. Wang, X. Wu, Y. Qiu, B. Guan, X. Xu, L. Fan, N. Zhang, K. Sun, MoN supported on graphene as a bifunctional interlayer for advanced Li-S batteries, Adv. Energy Mater. 9 (2019), 1901940.
[24] G. Jiang, F. Xu, S. Yang, J. Wu, B. Wei, H. Wang, Mesoporous, conductive molybdenum nitride as efficient sulfur hosts for high-performance lithium-sulfur batteries, J. Power Sources 395 (2018) 77–84.
[25] A. Habib, F. Florio, R. Sundararaman, Hot carrier dynamics in plasmonic transition metal nitrides, J. Opt. 20 (2018), 064001.
[26] L. Sui, X. Zhang, X. Cheng, P. Wang, Y. Xu, S. Gao, H. Zhao, L. Huo, Au-loaded hierarchical MoO3 hollow spheres with enhanced gas-sensing performance for the detection of BTX (Benzene, Toluene, And Xylene) and the sensing mechanism, ACS Appl. Mater. Interfaces 9 (2017) 1661–1670.
[27] S. Huang, Y.V. Lim, X. Zhang, Y. Wang, Y. Zheng, D. Kong, M. Ding, S.A. Yang, H. Y. Yang, Suppression of interdiffusion-induced voiding in oxidation of copper nanowires with twin-modified surface, Nano Energy 51 (2018) 340–348.
[28] H. Yuan, H.-J. Peng, B.-Q. Li, J. Xie, L. Kong, M. Zhao, X. Chen, J.-Q. Huang, Q. Zhang, Conductive and catalytic triple-phase interfaces enabling uniform nucleation in high-rate lithium-sulfur batteries, Adv. Energy Mater. 9 (2019), 1802768.
[29] X. Feng, K. Jiang, S. Fan, M.W. Kanan, Grain-boundary-dependent CO_2 electroreduction activity, J. Am. Chem. Soc. 137 (2015) 4606–4609.
[30] X. Feng, K. Jiang, S. Fan, M.W. Kanan, A direct grain-boundary-activity correlation for CO electroreduction on Cu nanoparticles, ACS Cent. Sci. 2 (2016) 169–174.

[31] S. Chen, C. Pei, J. Gong, Insights into interface engineering in steam reforming reactions for hydrogen production, Energy Environ. Sci. 12 (2019) 3473–3495.
[32] Y. He, P. Tang, Z. Hu, Q. He, C. Zhu, L. Wang, Q. Zeng, P. Golani, G. Gao, W. Fu, Z. Huang, C. Gao, J. Xia, X. Wang, X. Wang, C. Zhu, Q.M. Ramasse, A. Zhang, B. An, Y. Zhang, S. Martí-Sánchez, J.R. Morante, L. Wang, B.K. Tay, B.I. Yakobson, A. Trampert, H. Zhang, M. Wu, Q.J. Wang, J. Arbiol, Z. Liu, Engineering grain boundaries at the 2D limit for the hydrogen evolution reaction, Nat. Commun. 11 (2020) 57–68.
[33] Q. Pang, D. Kundu, M. Cuisinier, L.F. Nazar, Surface-enhanced redox chemistry of polysulphides on a metallic and polar host for lithium-sulphur batteries, Nat. Commun. 5 (2014) 4759–4766.
[34] B. Zhang, C. Luo, Y. Deng, Z. Huang, G. Zhou, W. Lv, Y.B. He, Y. Wan, F. Kang, Q. H. Yang, Alcohol oxidation: air-assisted transient synthesis of metastable nickel oxide boosting alkaline fuel oxidation reaction (Adv. Energy Mater. 46/2020, Adv. Energy Mater. 10 (2020), 200091.
[35] F.Y. Fan, W.C. Carter, Y.M. Chiang, Mechanism and kinetics of Li2S precipitation in lithium-sulfur batteries, Adv. Mater. 27 (2015) 5203–5209.
[36] M. Zhao, X.-Y. Li, X. Chen, B.-Q. Li, S. Kaskel, Q. Zhang, J.-Q. Huang, Promoting the sulfur redox kinetics by mixed organodiselenides in high-energy-density lithium–sulfur batteries, eScience (2021), https://doi.org/10.1016/j.esci.2021.08.001.
[37] M. Zhao, X. Chen, X.Y. Li, B.Q. Li, J.Q. Huang, An organodiselenide comediator to facilitate sulfur redox kinetics in lithium-sulfur batteries, Adv. Mater. 33 (2021), e2007298.
[38] Y. Li, G. Chen, J. Mou, Y. Liu, S. Xue, T. Tan, W. Zhong, Q. Deng, T. Li, J. Hu, C. Yang, K. Huang, M. Liu, Cobalt single atoms supported on N-doped carbon as an active and resilient sulfur host for lithium–sulfur batteries, Energy Storage Mater. 28 (2020) 196–204.
[39] Z. Li, Y. Zhou, Y. Wang, Y.-C. Lu, Solvent-mediated Li2S electrodeposition: a critical manipulator in lithium-sulfur batteries, Adv. Energy Mater. 9 (2019), 1802207.
[40] B.Q. Li, L. Kong, C.X. Zhao, Q. Jin, X. Chen, H.J. Peng, J.L. Qin, J.X. Chen, H. Yuan, Q. Zhang, J.Q. Huang, Expediting redox kinetics of sulfur species by atomic-scale electrocatalysts in lithium–sulfur batteries, InfoMat 1 (2019) 533–541.
[41] J.L. Yang, S.X. Zhao, X.T. Zeng, Y.M. Lu, Gz Cao, Adv. Mater. Interfaces 7 (2019), 1902420.
[42] J.-L. Yang, S.-X. Zhao, Y.-M. Lu, X.-T. Zeng, W. Lv, G.-Z. Cao, ZnS spheres wrapped by an ultrathin wrinkled carbon film as a multifunctional interlayer for long-life Li–S batteries, J. Mater. Chem. A 8 (2020) 231–241.
[43] Z. Du, X. Chen, W. Hu, C. Chuang, S. Xie, A. Hu, W. Yan, X. Kong, X. Wu, H. Ji, L. J. Wan, Cobalt in nitrogen-doped graphene as single-atom catalyst for high-sulfur content lithium-sulfur batteries, J. Am. Chem. Soc. 141 (2019) 3977–3985.
[44] Y. Fu, Z. Wu, Y. Yuan, P. Chen, L. Yu, L. Yuan, Q. Han, Y. Lan, W. Bai, E. Kan, C. Huang, X. Ouyang, X. Wang, J. Zhu, J. Lu, Switchable encapsulation of polysulfides in the transition between sulfur and lithium sulfide, Nat. Commun. 11 (2020) 845–854.
[45] H. Pan, J. Chen, R. Cao, V. Murugesan, N.N. Rajput, K.S. Han, K. Persson, L. Estevez, M.H. Engelhard, J.-G. Zhang, K.T. Mueller, Y. Cui, Y. Shao, J. Liu, Protective effects of new Wenshen Shengjing Decoction on cyclosporine-induced impairment of testosterone synthesis and spermatogenic apoptosis, Nat. Energy 2 (2017) 813–820.